Available online at www.sciencedirect.com
ScienceDirect
Optical Materials 29 (2007) 1048–1054
OPTICAL Materials
www.elsevier.com/locate/optmat

Photoluminescence of CdSe and CdSe/CdO · nH_2O core/shell nanoparticles prepared in aqueous solution

Xingping Zhou [a,b,*], Zhiyu Shao [a], Yoshio Kobayashi [c], Xiaqin Wang [d], Noriaki Ohuchi [e], Motohiro Taketa [e], Atsuo Kasuya [b]

[a] Institute of Biological Sciences and Biotechnology, Donghua University, North Renmin Road 2999, Shanghai 201620, PR China
[b] Center for Interdisciplinary Research, Tohoku University, Aramaki aza Aoba, Sendai 980-8578, Japan
[c] Department of Chemical Engineering, Graduate School of Engineering, Tohoku University, Sendai 980-8579, Japan
[d] College of Material Science and Engineering, Donghua University, Shanghai 200051, PR China
[e] Graduate School of Medicine, Tohoku University, Sendai 980-8574, Japan

Received 14 November 2005; received in revised form 17 April 2006; accepted 18 April 2006
Available online 9 June 2006

Abstract

CdSe sols with different colors were prepared by simply mixing $CdSO_4$ and $NaSSeO_3$ solutions under $[Cd^{2+}]/[Se^{2-}]$ ratios of 2.0–0.4 at room temperature. The nanoparticles, with average sizes of 1.8–3.6 nm, showed relatively narrow photoemission peaks at 522–556 nm. The strongest photoluminescence with a FWHM of 35 nm was obtained under $[Cd^{2+}]/[Se^{2-}]$ ratio of 1.2. The possible mechanism for achieving the strongest photoluminescence was proposed. Photoluminescence of these particles was greatly increased by surface modification of cadmium (II) hydrous oxide. The photoluminescence of these core–shell particles was kept constant in the pH range of 8.0–10.0, but dramatically decreased with an obvious blue-shifted peak while the pH was lower than 8.0. In addition, the photochemical oxidation of CdSe nanoparticles was markedly inhibited after they were modified with cadmium hydrous oxide.

PACS: 68.65.Hb; 78.55.–m

Keywords: Photoluminescence (PL); CdSe; Cadmium (II) hydrous oxide; Surface modification; pH; Stability

1. Introduction

Recently, studies on semiconductor quantum dots (QDs) have caused wide interests in their preparation, properties, and applications. Due to the quantum confinement effect, small nanoparticles have shown unique physical and chemical properties when their size is close to or smaller than the dimensions of the exciton within the corresponding bulk materials [1–3].

Due to the potential and practical applications of cadmium selenide (CdSe) semiconductor nanoparticles with a suitable band gap (1.76 eV), the preparation of CdSe nanoparticles and photoproperties such as absorption and exciton luminescence processes have been extensively studied [2,4–6]. In particular, CdSe semiconductor quantum dots have greatly interested biologists and pharmaceutical scientists [7,8] because of their size-dependent emissions. The luminescence is produced upon the recombination of the charge carriers, which are generated by light absorption. For the practical application in medical fields, the chemical stability, photoluminescence (PL) intensity, and emission position of CdSe QDs are of great importance [7,8]. However, the quantum yields in most of these studies were below 1% [7,8] and CdSe particles prepared in aqueous

* Corresponding author. Address: Institute of Biological Sciences and Biotechnology, Donghua University, North Renmin Road 2999, Shanghai 201620, PR China. Tel.: +86 21 6779 2657; fax: +86 21 6779 2647.
E-mail address: xpzhou@dhu.edu.cn (X. Zhou).

0925-3467/$ - see front matter © 2006 Elsevier B.V. All rights reserved.
doi:10.1016/j.optmat.2006.04.003

solution were hardly detectable [9]. The reason was that the colloidal particles had a lot of defect sites where radiationless recombination of the charge carriers occurred. For such small particles, the PL efficiency of nanocrystals can be dramatically reduced by localized surface-trap states. Therefore, controlling the quantum dot surface is required for an increase in the quantum efficiency. Proper surface modification will remove the local trap sites from the surface, thus, significantly increasing the quantum yield of the excitionic emission. The photoluminescence could be enhanced if the semiconductor nanoparticles are properly modified or coated with materials of a higher band gap. This holds true for Cd_3As_2 modified with $N(Et)_3$ [9], CdTe with thioglycolic acid [10] or dodecylamine [11], CdSe with CdS [12,13], with ZnS [14] or with ZnSe [15], etc.

Synthesis of CdSe QDs from inorganic sources in aqueous phase is a simple, important, and conventional process that many scientists have made successfully [5,6,16–18]. It has been found that deposition of cadmium (II) hydrous oxide on CdS nanoparticles increases markedly the PL efficiency of CdS nanoparticles [19]. However, the effect of cadmium (II) hydrous oxide on the PL intensity of CdSe QDs is an understudied process and has only been explored through our previous work [20] in which cadmium (II) hydrous oxide in a cubic structure was found to greatly enhance the PL intensity by modifying CdSe particle surface. More work in needed to determine the effect of reactant concentrations on the photoluminescence of the newly-formed CdSe nanoparticles because it is still unknown. Moreover, there is no information on the effects of some other factors such as reactant concentrations, pH of suspension, and oxygen on the photoluminescence of the CdSe/CdO · nH_2O core–shell composite particles. The investigation of such effects is of great importance for preparing strongly luminescing CdSe nanoparticles and their practical applications.

In this work, a series of CdSe QD sols with different sizes and fairly strong photoluminescence emissions at different wavelengths was prepared at room temperature based on a simple chemical precipitation under different reactant concentrations. CdSe sols with different sizes were passivated with cadmium hydrous oxide, showing a great increase in PL intensity. Moreover, investigation for pH effect on their photoluminescence and the stabilization against photo-degradation were also carried out.

2. Experimental

2.1. Materials

Special grade reagents (Wako Pure Chemical Ind.) of cadmium sulfate ($CdSO_4 \cdot 8/3\,H_2O$, 99+%), selenium powder (Se, 99+%), sodium sulfite (Na_2SO_3), hydrochloric acid (HCl), sodium hydroxide (NaOH) and sodium citrate ($C_6H_5Na_3O_7 \cdot 2H_2O$) were used as received. Water was doubly-distilled and deionized to have an electrical resistance higher than 18 $M\Omega\,cm^{-1}$.

2.2. Preparation of the stable suspension of CdSe nanoparticles

The formation equation used was: $Cd^{2+} + 2OH^- + SeSO_3^{2-} \rightarrow CdSe + SO_4^{2-} + H_2O$.

The standard conditions for preparing CdSe nanoparticles were established at pH ca. 8.0 under $[Cd^{2+}]/[Se^{2-}]$ ratio of 1.2 from cadmium sulfate and sodium selenosulfate. The details have been shown in Section 2 of our previous work [20].

To explore the effect of reactant concentrations on the photoluminescence, CdSe nanoparticles were also prepared at $[Cd^{2+}]/[Se^{2-}]$ ratio of 2.0, 1.6, 1.0, 0.8, and 0.4 under otherwise standard conditions.

2.3. Deposition of cadmium (II) hydrous oxide on CdSe nanoparticle surface

To 12 ml of the above fairly stable CdSe suspension prepared under the standard conditions, 0.01 M NaOH and 0.01 M $CdSO_4$ were drop-wisely added with vigorous agitation. The photoluminescence was checked for every addition of 0.67×10^{-4} M $CdSO_4$ and addition of the $CdSO_4$ stopped after the PL intensity no longer increased. Finally, 45 ml of the mixture was obtained. The NaOH was used for maintaining pH at 8.3.

In order to investigate pH effect on the photoluminescence of cadmium (II) hydrous oxide-deposited CdSe nanoparticles, the pH was adjusted with 0.1 M HCl or NaOH solution and this CdSe/CdO · nH_2O sol was aged at room temperature. After 8 h, the UV spectrum and the photoluminescence under different pH were measured for comparison.

2.4. Optical measurements

UV spectrometry of CdSe nanoparticles in suspension before and after deposition of cadmium (II) hydrous oxide was conducted with an ultraviolet–visible spectrophotometer, Hitachi U-2000, where the light path was 1 cm. In addition, the photoluminescence of these particles was measured with a JASCO FP-750 Spectrofluorometer equipped with Xe Lamp. The quantum efficiency (QE) was obtained by comparison to Rhodamine 6G aqueous solution.

3. Results

3.1. Optical properties of CdSe nanoparticles with different sizes

Fig. 1(i) shows UV–visible absorption spectra of CdSe suspensions prepared under different $[Cd^{2+}]/[Se^{2-}]$ ratios with 0.006 M selenide ion at pH ca. 8.0 at room temperature. For measurements, all the suspensions were diluted by 15 times after the removal of the supernatants by centrifugation. As revealed from Fig. 1(i), with an increase in

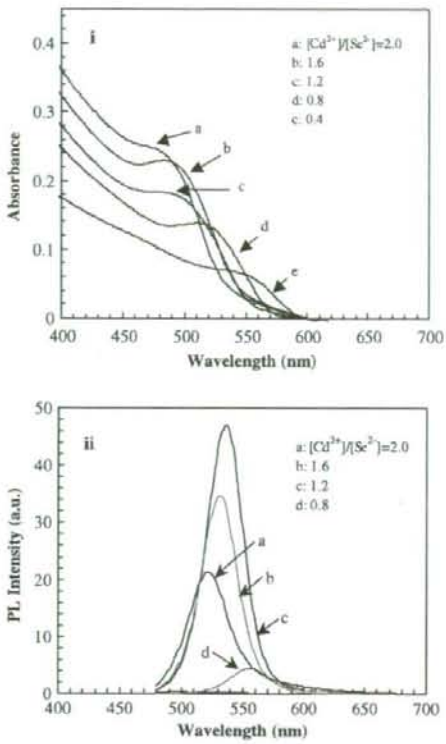

Fig. 1. (i) UV–visible spectra of CdSe suspensions formed at pH ~ 8.0 at room temperature under different ratios of $[Cd^{2+}]/[Se^{2-}]$ with 0.006 M Se^{2-}: (a) 2.0; (b) 1.6; (c) 1.2; (d) 0.8; (e) 0.4. (ii) Photoluminescence (PL) of CdSe suspensions whose UV spectra are shown in (i) (Exc. 400 nm).

Cd^{2+} concentration (from sample e to a), absorption shoulders ranged from 560 to 480 nm, which were blue-shifted from 712 nm of the bulk CdSe band gap. This is a strong evidence for quantum confinement effect in the CdSe nanocrystals. The out looking of the samples also exhibited the change in color from red to orange and then to yellow from sample e to a, which revealed that a series of nano-sized CdSe crystallines was successfully produced. Their corresponding particle sizes were 1.8 nm (a), 2.0 nm (b), 2.3 nm (c), 2.9 nm (d), and 3.6 nm (e), based on their absorption shoulder positions and XRD patterns [2,20].

Fig. 1(ii) displays the photoluminescence (PL) spectra (Exc. 400 nm) of the same samples in Fig. 1(i). A series of PL peaks was observed in the range of 555–520 nm for samples d–a. However, the photoluminescence was undetectable for the sample e under $[Cd^{2+}]/[Se^{2-}]$ ratio of 0.4. The strongest PL intensity was obtained in sample c under $[Cd^{2+}]/[Se^{2-}]$ ratio of 1.2.

Table 1 presents a summary of the average particle sizes and the photoluminescence characteristics. All the PL peaks had a full width at half maximum (FWHM) in the range of 35–40 nm. Consequently, the sample c which had the strongest PL intensity was also of the narrowest emission band among all the samples. This possibly was caused by the adsorption of the excessive Cd^{2+} onto CdSe nanoparticles and a nearly-optimized concentration of reactants in preparation. A greater explanation of the reasons this takes place will be provided in Section 4.

3.2. Enhancing photoluminescence of CdSe nanoparticles by surface deposition of cadmium (II) hydrous oxide

Fig. 2a displays the effects of the added $CdSO_4$ at pH ~ 8.3 on the photoluminescence of the CdSe sol ([CdSe]: $\sim 3.0 \times 10^{-4}$ M) prepared under $[Cd^{2+}]/[Se^{2-}]$ ratio of 1.2. The pH was adjusted with NaOH. Fig. 2b shows the relationship between PL intensity and the concentration of the added $CdSO_4$. The photoluminescence was enhanced greatly with the added $CdSO_4$ until 4.0×10^{-4} M $CdSO_4$. Then, there is no longer PL intensity increase at $[CdSO_4]$ larger than 4.0×10^{-4} M. According to the previous work [20], cubic cadmium hydrous oxide was formed on the CdSe particle surface which was also in the cubic structure. Thus, the enhanced PL intensity may result from the formation of the core–shell structure since the cadmium hydrous oxide shell was of a higher band gap than the CdSe core. The shell has the added benefit that it may possibly remove the defect sites on the surfaces produced in the formation process of the CdSe nanoparticles. Fig. 2c shows the relationship between PL position and the concentration of the added $CdSO_4$. It was found that the photoluminescence peak position was red-shifted from 539 nm to 544 nm while the $CdSO_4$ concentration increased to 4.0×10^{-4} M. Also, there is no longer a red-shifted position at $[CdSO_4]$ larger than 4.0×10^{-4} M. This suggests that the cadmium hydrous oxide shell is thick and rigid enough to remove the defect sites existing on

Table 1
Particle size and photoluminescence (PL) of CdSe prepared under different ratios of $[Cd^{2+}]/[Se^{2-}]$ at pH ~ 8.0 at room temperature

Run no.	$[Cd^{2+}]/[Se^{2-}]$ ($[Se^{2-}] = 0.006$ M)	Average particle size (nm)	PL peak position (nm)	FWHM (nm)	QE (%)
a	2.0	1.8	522	39	1.5
b	1.6	2.0	531	36	2.5
c	1.2	2.3	539	35	3.1
d	0.8	2.9	556	40	0.4
e	0.4	3.6	–	–	–

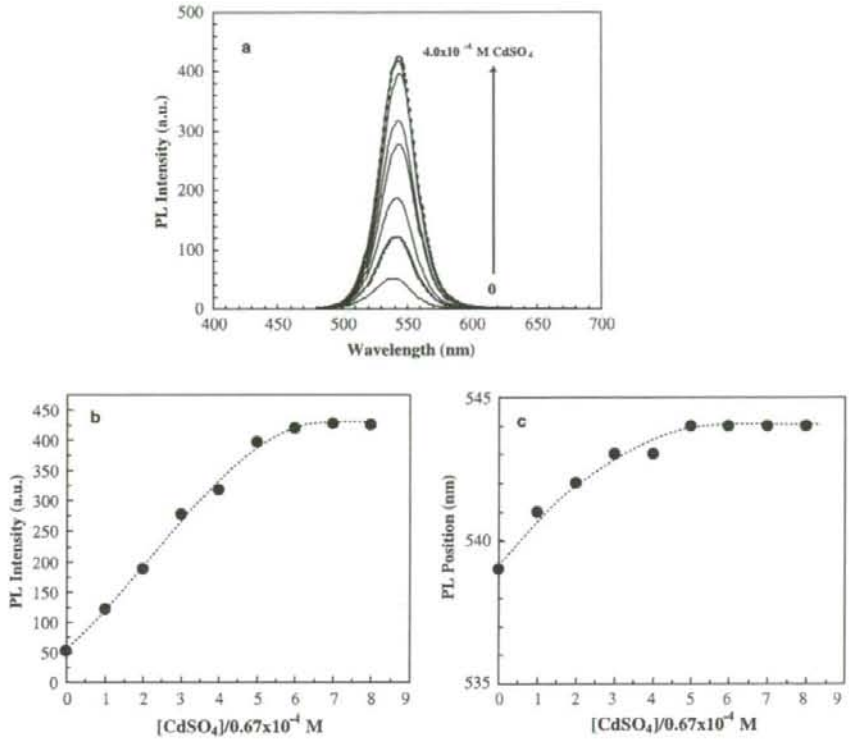

Fig. 2. (a) Effect of cadmium (II) hydrous oxide deposition on the CdSe surfaces on their photoluminescence; (b) Effect of the added $CdSO_4$ on PL intensity. (c) Effect of the added $CdSO_4$ on PL position.

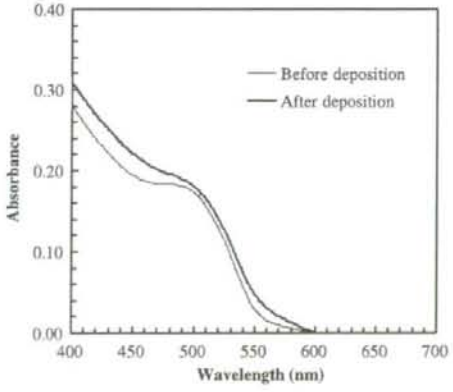

Fig. 3. UV–visible spectra of the CdSe suspension before and after cadmium hydrous oxide deposition (added $[CdSO_4] = 4.0 \times 10^{-4}$ M).

CdSe surfaces. Fig. 3 shows the UV spectra of the CdSe sols with and without addition of 4.0×10^{-4} M of $CdSO_4$. The absorption shoulder was slightly red-shifted after the addition of $CdSO_4$ probably due to quantum confinement effect. This could result in the red-shifted photoluminescence shown in Fig. 2.

3.3. Effect of pH on the photoluminescence of $CdSe/CdO \cdot nH_2O$ core/shell nano-composites

The pH effect on the photoluminescence of CdSe/$CdO \cdot nH_2O$ core/shell nano-composite sols was studied by adjusting the pH of these sols with 0.1 M HCl or NaOH. Fig. 4a–c illustrate the responding changes in PL intensity, PL peak position, and UV spectra under different pH, respectively. In Fig. 4a, the PL intensity was fairly stable in the pH range of 8.0–10.0. In contrast, the PL intensity dramatically decreased with a decrease in pH while pH < 8.0, this may be related to the change in morphology of the cadmium hydrous oxide shell at a different pH. Interestingly, PL intensity was mostly recovered if the pH was increased again. In the case of pH > 10.0, the normal coagulation of the particles took place. From Fig. 4b, the PL peak position was greatly blue-shifted with a decrease in pH from 8.0. This may also be due to the change in morphology of the shell because it made the particles smaller. In the pH range of 8.0–10.0, the peak position was also constant, revealing that there was no observable effect of

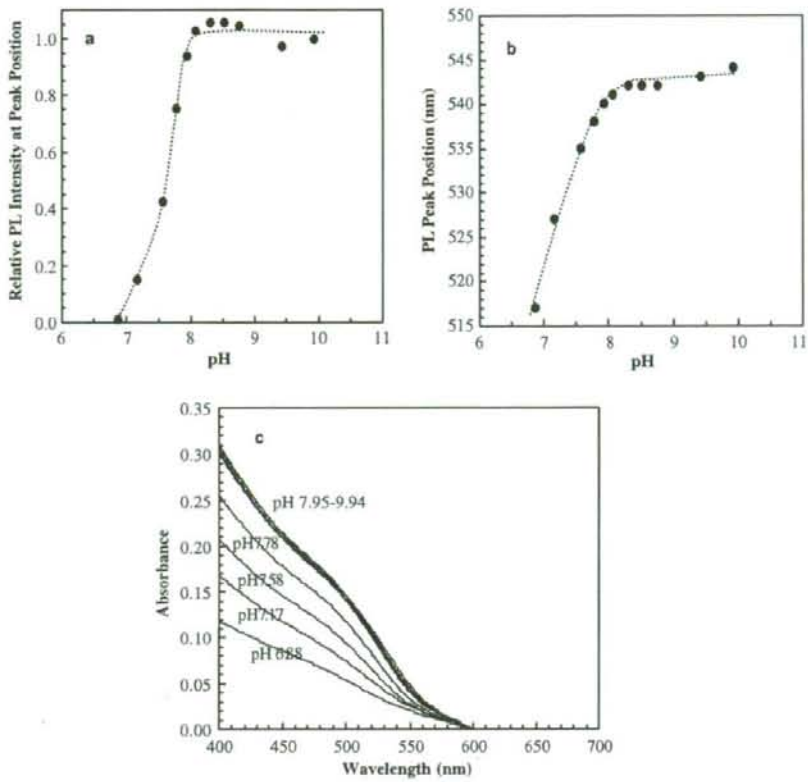

Fig. 4. (a) pH Effect on PL intensity of the CdSe/CdO · nH_2O core–shell nano-composites at the peak position. (b) pH effect on the peak position. (c) UV spectra of CdSe/CdO · nH_2O core–shell nano-composites aged under different pH.

the adsorbed OH^- on the shell of the composite particles on their photoluminescence in such a system with excessive hydroxide ions. Fig. 4c further confirmed the above descriptions. Similarly, the absorption intensity was also recovered after the pH was increased again.

3.4. Stabilization of CdSe/CdO · nH_2O core/shell composite nanoparticles against photo-degradation

Fig. 5 illustrates the time evolution of UV absorbance of the CdSe nanoparticles prepared under $[Cd^{2+}]/[Se^{2-}]$ ratio of 1.2 and that of the CdSe/CdO · nH_2O nano-composites. After deposition of cadmium hydrous oxide on the particle surfaces, the absorbance was kept constant. However, the absorbance of CdSe nanoparticles without deposition treatment decreased noticeably after several days. These findings reveal that the deposition of cadmium hydrous oxide also prevented O_2 from reaching Se^{2-} existing on the surface of CdSe particles. Here, the cadmium hydrous oxide played a role similar to the shell of ZnS [14] and SiO_2 [18] around CdSe cores. With the shell, CdSe particles became chemically inactive and then kept the absorbance constant. For the composite nanoparticles, the photoluminescence was also kept constant due to the same reason.

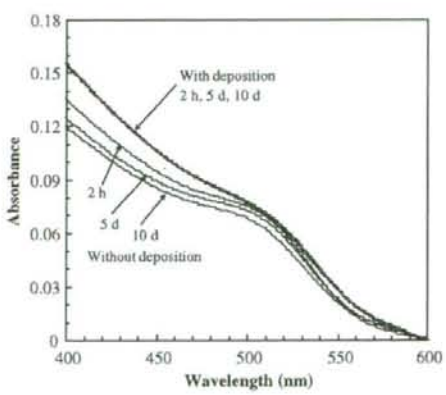

Fig. 5. UV–visible spectra at different times after preparation of CdSe nanoparticles (—) under $[Cd^{2+}]/[Se^{2-}]$ ratio of 1.2 and the nanoparticles modified with cadmium hydrous oxide (–).

Table 2
Photoluminescence (PL) enhancement of CdSe nanoparticles prepared under different conditions by surface deposition of cadmium (II) hydrous oxide at pH ~ 8.3

$[Cd^{2+}]/[Se^{2-}]$	$[Se^{2-}]$ (M)	Average particle size (nm)	PL peak position (nm)		QE (%)	
			Before[a]	After[a]	Before[a]	After[a]
1.2	0.006	2.3	539	544	3.1	34.8
0.8	0.006	2.9	556	565	0.4	3.4
1.2	0.002	3.6	597	608	0.1	2.5

[a] This means before or after deposition of cadmium (II) hydrous oxide.

3.5. Effect of deposited cadmium (II) hydrous oxide on photoluminescence of CdSe sols prepared under some other conditions

The effect of cadmium hydrous oxide shell on the photoluminescence was also explored at pH ~ 8.3 for the CdSe nanoparticles prepared under $[Cd^{2+}]/[Se^{2-}]$ ratio of 0.8 with 0.006 M Se^{2-} and $[Cd^{2+}]/[Se^{2-}]$ ratio of 1.2 with 0.002 M Se^{2-}. The results are summarized in Table 2.

After deposition of cadmium hydrous oxide on such nanoparticles, all the quantum efficiencies were greatly increased and the PL peak positions were all red-shifted. This reveals that the PL intensity of all the particles prepared in such a system at room temperature can be enhanced by surface modification with deposition of cadmium hydrous oxide.

Moreover, under $[Cd^{2+}]/[Se^{2-}]$ ratio of 1.2, it was found that the particle became larger and the QE became lower while $[Se^{2-}]$ was lowered from 0.006 M to 0.002 M during preparation. The possible reasons will be also provided in Section 4.

4. Discussion

4.1. Cadmium (II) hydrous oxide shell and photoluminescence

It has been found that only the cadmium hydrous oxide deposited on the surfaces of CdSe nanoparticles can promote the photoluminescence of CdSe sol [20]. The effect of the cadmium hydrous oxide shell is so strong that even $Cd^{2+}\cdots OH^-$ formed on the particle surface can apparently increase the PL intensity. It should be noted that it is difficult for the formation of $Cd^{2+}\cdots OH^-$ to take place on the surface of CdSe with a Se^{2-} rich or Cd^{2+} poor surface.

In the current formation system, when $[Cd^{2+}]/[Se^{2-}] > 1.0$, the particles were formed basically with Cd^{2+} rich surfaces. This suggests there is a possibility for the formation of cadmium hydrous oxide on the CdSe surface in a weak alkaline system. The PL intensity can be promoted by modifying the particle surface from Cd^{2+} poor to Cd^{2+} rich as shown in Fig. 4 of the previous work [20]. Therefore, the increasing PL intensity from the sample d to c in Table 1 may be due to the formation of $Cd^{2+}\cdots OH^-$ or a very thin shell of cadmium hydrous oxide on the CdSe particle surface. However, the PL intensity decreased from the sample c to a in Table 1 when $[Cd^{2+}]/[Se^{2-}]$ got much higher than 1.0. Since concentrated electrolytes often increases the defect sites on the surfaces of nanoparticles, this decreasing photoluminescence may be explained in the existence of a high concentrated electrolyte caused by the addition of a large amount of $CdSO_4$ in order to make the high ratio of $[Cd^{2+}]/[Se^{2-}]$.

Based on the above descriptions, one should be able to understand the reasons why there is a key factor for preparing the particles with the strongest PL intensity. Such behaviors are also found in other colloidal systems such as aqueous preparation of CdTe nanoparticles with different sizes and the strongest PL intensity at 540 nm [21].

On the other hand, although the photoluminescence of the nanoparticles formed in the current system can always be greatly promoted by surface modification with cadmium hydrous oxide, the final PL QE of the modified CdSe particles is mainly controlled by that of the un-modified ones as displayed in Table 2. So, there should be some other important factors affecting the QE of CdSe nanoparticles, which are independent to the deposition. They may be reactant concentrations and the concentration ratio in particle preparation.

4.2. Reactant concentration, particle size, and photoluminescence

As CdSe nanoparticles prepared in aqueous solution usually have a weak luminescence, it is important from the viewpoint of colloid preparation that conditions have been found in this study that demonstrate that CdSe sols with a fairly strong photoluminescence can be made. The crucial factors in the preparation are the precursor concentration and the ratio of $[Cd^{2+}]/[Se^{2-}]$. In Table 1, the particle size increased with a decrease in ratio of $[Cd^{2+}]/[Se^{2-}]$. From Table 2, under the same ratio of $[Cd^{2+}]/[Se^{2-}]$, the formed particle became large while $[Se^{2-}]$ decreased. Actually, for such a typical colloidal formation system, the particle size was determined by precursor concentrations. To summarize, large particles are often obtained at a low precursor concentration.

On the other hand, Ostwald ripening often takes place in colloidal solutions. Consequently, Ostwald ripening becomes more efficient while the solute concentration becomes low due to the relatively low free solute ions [22]. However, the choice of low concentration increases the average surface disorder of nanocrystals, therefore, results in quenching of photoluminescence. Hence, in aqueous solutions large particles formed at a low solute concentration usually have a small QE. Hereafter, it becomes more difficult for producing large particles with a strong emission at a long wavelength. Therefore, in Table 1 from the sample d to e and in Table 2 for CdSe nanoparticles prepared under $[Cd^{2+}]/[Se^{2-}]$ ratio of 1.2 with Se^{2-} ions from 0.006 M to 0.002 M, the decreased photoluminescence may be due to the more efficient Ostwald ripening

under relatively diluted reactants. CdTe nanoparticles prepared in aqueous solution showed the same behaviors [21].

5. Conclusions

CdSe quantum dots with average sizes of 1.8–3.6 nm were prepared under $[Cd^{2+}]/[Se^{2-}]$ ratios of 2.0–0.4 in aqueous solution and showed a relatively narrow photo emission peak at 522–556 nm. The strongest photoluminescence was obtained under $[Cd^{2+}]/[Se^{2-}]$ ratio of 1.2 due to the combination effects of modification of cadmium hydrous oxide, Ostwald ripening, and electrolytes.

The photoluminescence of CdSe nanoparticles was greatly promoted by surface deposition of cadmium hydrous oxide. The photoluminescence of the core–shell structured CdSe/CdO · nH_2O nano-composites was kept stable in the pH range of 8.0–10.0.

The shell of cadmium hydrous oxide was rigid enough to prevent O_2 to oxidize Se^{2-} and then stabilized CdSe nanoparticles against photo degradation.

Acknowledgements

The authors gratefully thank the Welfare Department of the Japanese Government and Donghua University for their support through a research fund that made this research possible.

References

[1] A. Henglein, Chem. Rev. 89 (1989) 1861.
[2] C.B. Murray, D.J. Norris, M.G. Bawendi, J. Am. Chem. Soc. 115 (1993) 8706.
[3] D.L. Klein, R. Roth, A.K.L. Lim, A.P. Alivisatos, P.L. McEuen, Nature 389 (1997) 699.
[4] J.E.B. Katari, V.L. Colvin, A.P. Alivisatos, J. Phys. Chem. 98 (1994) 4109.
[5] S. Gorer, G. Hodes, J. Phys. Chem. 98 (1994) 5338.
[6] E. Lifshitz, I. Dag, I. Litvin, G. Hodes, S. Gorer, R. Reisfeld, M. Zelner, H. Miuti, Chem. Phys. Lett. 288 (1998) 188.
[7] M. Bruchez Jr., M. Moronne, P. Gin, S. Weiss, A.P. Alivisatos, Science 281 (1998) 2013.
[8] W.C.W. Chan, S. Nie, Science 281 (1998) 2016.
[9] T. Dannhauser, M. O'Neil, K. Johansson, D. Whitten, G. McLendon, J. Phys. Chem. 90 (1986) 6074.
[10] M. Gao, S. Kirstein, H. Möhwald, Andrey L. Rogach, A. Kornowski, A. Eychmueller, H. Weller, J. Phys. Chem. B 102 (1998) 8360.
[11] D.V. Talapin, A.L. Rogach, I. Mekis, S. Haubold, A. Kornowski, M. Haase, H. Weller, Colloids Surf. A: Physicochem. Eng. Aspects 202 (2002) 145.
[12] X. Peng, M.C. Schlamp, A.V. Kadanich, A.P. Alivisatos, J. Am. Chem. Soc. 119 (1997) 7019.
[13] S. Liu, H. Guo, Z. Zhang, R. Li, W. Chen, Z. Wang, Physica E 8 (2000) 174.
[14] B.O. Dabbousi, J. Rodriguez-Viejo, F.V. Mikulec, J.R. Heine, H. Mattoussi, R. Ober, K.F. Jensen, M.G. Bawendi, J. Phys. Chem. B 101 (1997) 9463.
[15] P. Reiss, S. Carayon, J. Bleuse, A. Pron, Synth. Met. 139 (2003) 649.
[16] A.L. Rogach, D. Nagesha, J.W. Ostrander, M. Giersig, N.A. Kotov, Chem. Mater. 12 (2000) 2676.
[17] L. Xu, K. Chen, J. Zhu, H. Chen, H. Huang, J. Xu, X. Huang, Superlattices Microstruct. 29 (2001) 67.
[18] X.P. Zhou, Y. Kobayashi, V. Romanyuk, N. Ohuchi, M. Takeda, S. Tsunekawa, A. Kasuya, Appl. Surf. Sci. 242 (3–4) (2005) 281.
[19] L. Spanhel, M. Haase, H. Weller, A. Henglein, J. Am. Chem. Soc. 109 (1987) 5649.
[20] X.P. Zhou, Y. Kobayashi, N. Ohuchi, M. Takeda, A. Kasuya, Int. J. Modern Phys. B 19 (15–17) (2005) 2835.
[21] H. Zhang, L. Wang, H. Xiong, L. Hu, B. Tong, W. Li, Adv. Mater. 15 (2003) 1712.
[22] D.A. Talapin, A.L. Rogach, E.V. Shevchenko, A. Kornowski, M. Haase, H. Weller, J. Am. Chem. Soc. 124 (2002) 5782.

Fluorescence Tomography of Biological Tissue Based on Ultrasound Tagging Technique

Masaki Kobayashi*[a], Takashi Mizumoto[a], Trinh Quang Duc[a], Motohiro Takeda[b, c]
[a] Department of Electronics, Tohoku Institute of Technology, Sendai 982-8577, Japan;
[b]Department of Bioengineering and Robotics, Graduate School of Engineering, Tohoku University, Sendai 980-8579, Japan; [c]Division of Surgical Oncology, Graduate School of Medicine, Tohoku University, Sendai 980-8579, Japan

ABSTRACT

We report a study for the development of tomographic imaging technique of fluorescence in biological tissue for assays of biological function. Ultrasonic modulation of light based on the acousto-optic effect (so called ultrasound 'tagging') is applied for imaging of fluorescence distribution in the light-scattering media. Sound-field characteristics that affect the light by modulating its amplitude through variation of the refractive index in the medium were determined. With using focused ultrasound, selectively modulated fluorescence on a depth-axis of the medium can be detected. Ultrasound tagging technique applied measuring the optical absorption in light scattering media is well known, and it is principally based on the modulation of speckle pattern. On the contrary, in the case of fluorescence, displacement of scattering particles and variation of the refractive index that is induced by density distribution in a sound field might produce the intensity modulation of scattered light. We have experimentally shown that ultrasound tagging technique is also available for fluorescence measurement. In this paper, we demonstrate the result of tomographic images of fluorescence in dense scattering media using porcine muscle as a biological tissue, and bovine adipose. Tissue samples had the dimension of 40 x 40 mm in section and fluorophore which had the 3mm size was embedded in the center of the tissue. The localized image of the fluorophore was determined with the spatial resolution of focus size of the ultrasound, suggesting the applicability of this technique for visualization of fluorescent probes in deep portion of living body.

Keywords: fluorescence , imaging, acoustooptic effect, ultrasound, laser, tomography, turbid medium, scattering

1. INTRODUCTION

Fluorescence imaging techniques for the analysis of biological functions using fluorescent probes that label physiological molecules are an essential tool in the field of life science. Recently, quantum dots, which have excellent optical performance, have been widely used as new fluorescent probes, and are also anticipated to be applied for clinical use. Fluorescent probes for bioassay have the advantage of dynamics visualization of bio-functions in real-time with low invasion. However, the light-scattering in biological tissues restricts the applicability of fluorescence imaging of living bodies inside. A great deal of effort has been devoted to develop the optical imaging technique for living bodies [1]. Those efforts have made improve the technique of characterization of optical properties even in light scattering media. Recently, the 'tagging' technique using the interaction of light with ultrasound has been widely studied for exploring the novel technique to determine the optical absorption in biological tissue [2]. In the case of absorption determination using tagging technique, the intensity modulation in a varying sound-pressure field is caused by the variation of speckle pattern formed in multiply scattered coherent light. We have examined the feasibility of the application of tagging technique for fluorescence imaging. In the case of fluorescence, the displacement of scattering particles and variation of the refractive index induced by density distribution in a sound field might also generate the intensity modulation [3]. We have already demonstrated the availableness of this technique for fluorescence imaging with using tissue phantoms under the condition of 532nm excitation [4]. Here, we demonstrate tomographic imaging of fluorescence in biological tissue in which fluorofore is locally embedded in the center of the tissue.

* masaki@tohtech.ac.jp; phone 81 22 305-3211; fax 81 22 305-3202

Biophotonics 2007: Optics in Life Science, edited by Jürgen Popp, Gert von Bally, Proc. of SPIE-OSA Biomedical Optics, SPIE Vol. 6633, 663306, © 2007 SPIE-OSA · 1605-7422/07/$18

2. MATERIALS AND METHODS

2.1 Experimental setup

Figure 1 shows that the experimental setup. A continuous wave (CW) Ti:sapphire laser system pumped with a diode pumped solid state (DPSS) laser (Verdi V-6; Coherent Inc.) is used as light source for excitation. The laser beam is reduced and collimated, and goes through the glass window on the side wall of a water tank. A focus-type ultrasonic transducer (38 mm focal length, 3 mm focal diameter, V314-SU; Olympus-NDT) that is driven by a 1 MHz continuous sinusoidal wave is incorporated into the side wall of the water tank, where the ultrasound beam traverses the incident axis of the laser beam. Sound pressure in the sound-field focus region was 4.1×10^4 Pa in water. A photomultiplier tube (PMT) is placed by the opposite side of the window of incident beam. The signal from the PMT is fed into a spectrum analyzer and the intensities of the resonant frequencies are detected using a narrow bandwidth (100Hz). To obtain a two-dimensional tomographic image of fluorescence intensity through scanning of the ultrasound focus, a water tank equipped with a transducer is mounted on a three-axis translational stage and scanned in 500 μm steps along the X-axis (parallel to the incident laser beam) and the Y-axis (parallel to the ultrasound beam). Total scanning area is 20 × 20 mm. It is controlled using a personal computer via GP-IB interface that is synchronized with a spectrum analyzer. The entire control program was written in Lab windows (National Instruments Co., USA).

A sample for the measurement (tissue phantoms or biological tissues) is put in an acrylic holder and suspended from the outside of the water tank. The sample with acrylic holder is immersed in the water. The optical arrangement of the sample and incident laser beam remains unchanged during scanning of the ultrasound beam which is from the side wall of the water tank. The imaging experiments are conducted using a wavelength of 726 nm and an incident beam signal intensity of 40 mW. The light modulation mechanism is inferred to be induced through density variation of the medium in the ultrasound field, which engenders changes of the refractive index and optical scattering coefficient. When fluorescent pigment is present in the sound field, the density variation of the medium engenders modulation of the photon density through deflection of light between two successive scattering events in the gradient of the refractive index, thereby causing fluorescence intensity modulation. Variation of the scattering coefficient may also cause modulation of the fluorescence intensity.

Characteristics of fluorescence modulation intensity as a function of sound pressure measured under the condition in which ultrasound focuses on the fluorescent region site in the scattering medium shows that fluorescence modulation (signal) intensity is proportional to the square of the sound pressure, indicating a linear relationship between the sound power and the fluorescence signal intensity [4].

2.2 Sample

As a tissue phantom, we fabricated isotropic light-scattering gel made of 5% agar (Inagel; Ina Food Industry Co. Ltd., Nagano, Japan) that were prepared through dilution of Intralipid (Intralipid-10%; Fresenius Kabi AG, Germany). The final volume concentration of Intralipid in the phantom was 80 ml/l in 5% agarose gel with the water-glycerin (20%) solution. The agarose gel was molded to 40 × 40 × 75 (height) mm. A fluorescent region in the phantom was formed by embedding a fluorescent material that contains fluorescent microspheres (715 nm absorption peak, 755 nm emission wavelength; carboxylate-modified microspheres, FluoSheres F-8799, Molecular Probes Inc., USA) molded with columnar agarose gel (5 mm long, 3 mm diameter).

A tissue of porcine muscle purchased from a supermarket is used as a biological tissue sample. It is cut and formed with 40 × 40 × 75 mm, and drilled at the center of the tissue. Fluorescent microspheres (FluoSheres F-8799) molded with columnar capsule (5 mm long, 3 mm diameter) is embedded in the center of the tissue.

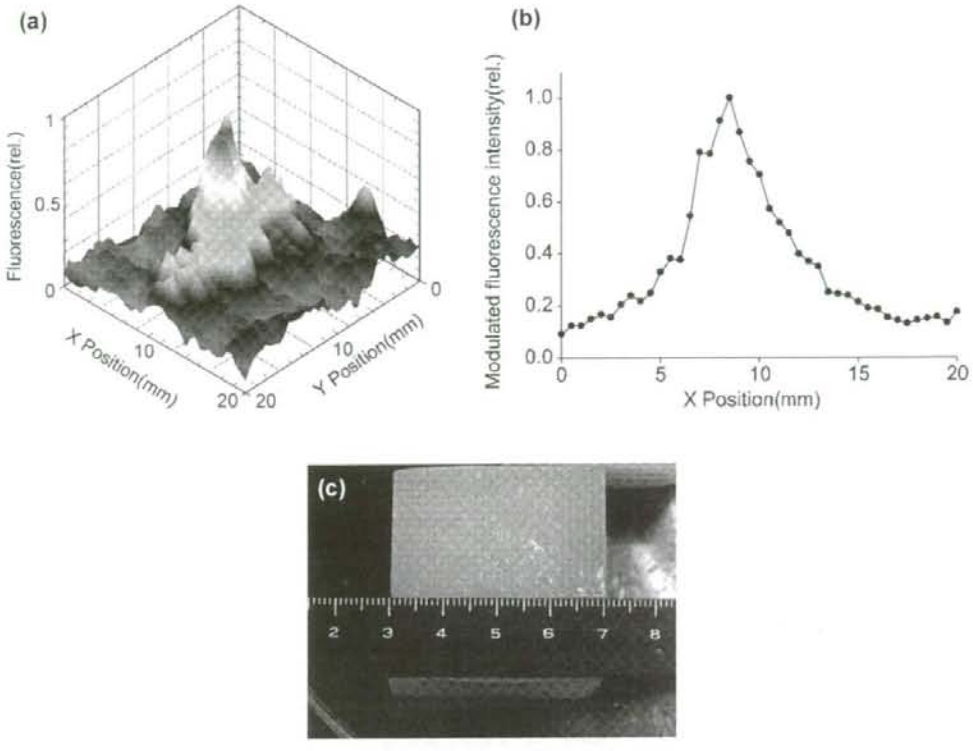

Fig. 2 (a) A tomographic image of fluorescence observed with a tissue phantom of light-scattering gel with a single fluorescent region in the phantom's center. (b) A profile of the signal intensity along with X-axis on the image sectioned at the center of the phantom, which contains the embedded fluorescent region. (c) A top view of a tissue phantom with a scale showing the dimension. Embedded region of fluorophore is in the centre of the phantom.

3.2 Tomographic image obtained with using a porcine muscle which has a fluorophore in the centre

A tomographic image of fluorescence observed with a porcine muscle that contains a localized fluorescent region in the center is shown in Fig. 3 (a). A localized area of fluorophore at the center of the tissue is detected. The area of higher signal intensity corresponds to the region of fluorophore embedded in the sample. The profile of the signal intensity along the X-axis on the image sectioned at the center of the phantom including the fluorescent region is indicated in Fig. 3 (b). The peak width of the profile is *ca.* 3 mm in the full-width at half-maximum. It matches the diameter of the embedded fluorescent region and the size of ultrasound focus. A photograph of tissue sample inserted in a holder is shown in Fig. 3(c). With consideration of the signal-to-noise ratio obtained in this experiment and scattering coefficient of the living tissue, this result suggests the potential of this technique for imaging of fluorescence buried in biological tissues with *ca.* 30mm depth. Considering this, further progress in the development of scanning techniques, for example using an arrayed ultrasound transducer, can provide a method for measuring fluorescence in bodies for clinical use. This technique is expected to facilitate the expansion of fluorescent probes' use for biological applications throughout the fields of life science and clinical medicine.

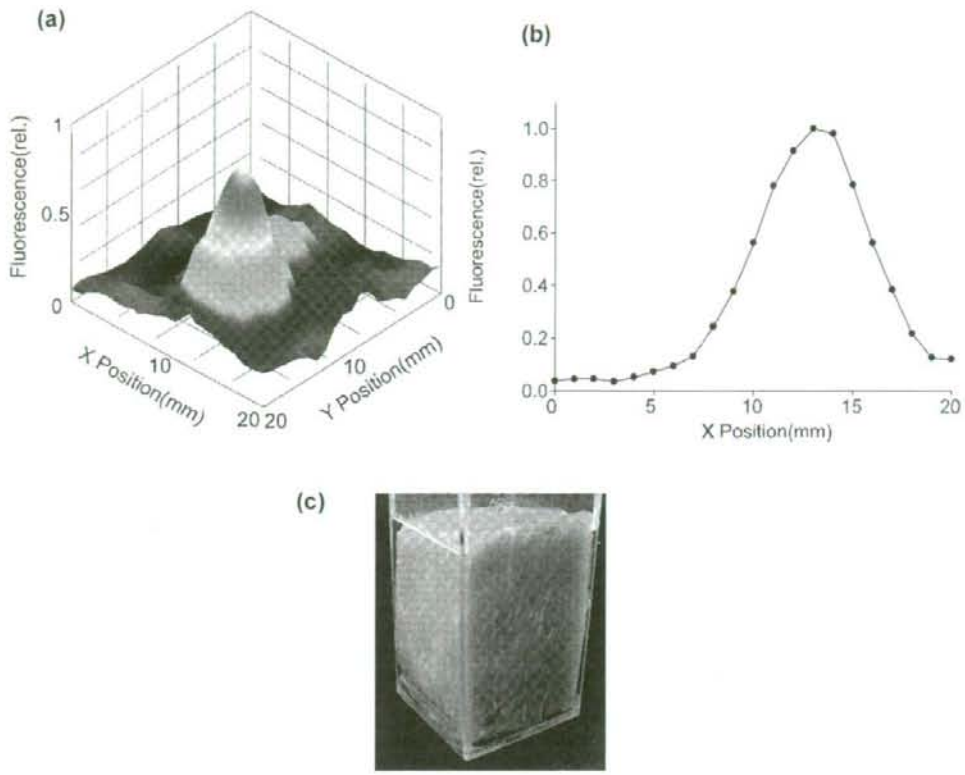

Fig. 3. (a) A tomographic image of fluorescence observed with a porcine muscle with a single fluorescent region in the phantom's center. (b) A profile of the signal intensity along with X-axis on the image sectioned at the center of the tissue, which contains the embedded fluorescent region. (c) An aspect of a tissue sample with a holder.

REFERENCES

1. T. Vo-Dinh ed., *Biomedical Photonics Handbook*, CRC Press, Boca Raton, (2003).
2. L. V. Wang, S. L. Jacques, and X. Zhao, "Continuous-wave ultrasonic modulation of scattered laser light to image objects in turbid media," *Opt. Lett.* 20, 629 (1995).
3. M. Kobayashi, T. Kasamatsu, Y. Shibuya, M. Enomoto, "Optical visualization of ultrasound pressure fields in turbid media based on a coherent detection imaging technique," *Jpn. J. Appl. Phys.* 45, 1836 (2006).
4. M. Kobayashi, T. Mizumoto, Y. Shibuya, M. Enomoto, M. Takeda, "Fluorescence tomography in turbid media based on acousto-optic modulation imaging", *Appl. Phys. Lett.* 89, 181102 (2006).

Journal of
Nanoscience and Nanotechnology
Vol. 7, 2690–2695, 2007

Concentrated Colloids of Silica-Encapsulated Gold Nanoparticles: Colloidal Stability, Cytotoxicity, and X-ray Absorption

Yeon-Su Park[1,*], Atsuo Kasuya[1,*], Andriy Dmytruk[1], Noda Yasuto[1], Motohiro Takeda[2], Noriaki Ohuchi[3], Yoshinori Sato[4], Kazuyuki Tohji[4], Motohiro Uo[5], and Fumio Watari[5]

[1]Center for Interdisciplinary Research, Tohoku University, Aoba-ku, Sendai 980-8578, Japan
[2]Department of Bioengineering and Robotics, Tohoku University, Aoba-ku, Sendai 980-8579, Japan
[3]Division of Surgical Oncology, Graduate School of Medicine, Tohoku University, Aoba-ku, Sendai 980-8574, Japan
[4]Graduate School of Environmental Studies, Tohoku University, Aoba-ku, Sendai 980-8579, Japan
[5]Graduate School of Dental Medicine, Hokkaido University, Kita-ku, Sapporo 060-8589, Japan

As an effort to develop a new, effective, nontoxic X-ray contrast agent, the concentrated colloids of silica-encapsulated gold nanoparticles (Au@SiO_2 NPs) were fabricated and their colloidal stability, cytotoxicity, and X-ray absorption were investigated. The concentrated colloidal NPs were manufactured by forming a 4 nm-thick silica shell on the surface of each Au NP with 15 nm diameter, followed by enrichment to [Au] = 100 mM. They were very stable in water: the NPs were well separated each other without forming agglomerates and their optical property was very similar to that before enrichment. The colloidal stability of the NPs in biological environment was strongly dependent on their previous morphology in water. The NPs with minor shell damage were stable in phosphate buffered saline (PBS) solution: both in water and in PBS solution, they showed very similar morphology and optical property. However, the NPs with profound shell damage formed big agglomerates in PBS solution, resulting in the red-shift and broadening of the Au surface plasmon resonance peak. Cell viability and proliferation assessments revealed the biocompatibility of the Au@SiO_2 NPs: no apparent cytotoxicity was observed even at 100 ppm NPs. The concentrated colloidal NPs showed very strong X-ray absorption. Their relative X-ray transmittance to water was comparable to that of a commercial agent. Considering these, the concentrated colloids of the Au@SiO_2 NPs are suitable for an X-ray contrast agent.

Keywords: Gold, Silica, X-ray Absorption, Cytotoxicity, Colloidal Stability.

1. INTRODUCTION

As concerns on human health increase tremendously in modern society, there have been strong demands for more effective and safer medical diagnoses. One of the most indispensable modern diagnostic tools is a computed tomography (CT), which strongly relies on the contrast ability of X-ray contrast agents. Currently, tri-iodobenzene derivatives are extensively used as the contrast agents. However, sometimes these iodine-containing small organic molecules cause some serious problems such as limited imaging time, due to their short vascular circulation time, and renal toxicity. Thus, CT practices occasionally require intra-arterial catheterization which may impose serious health risks. In these regards, there have been ceaseless efforts to develop more effective and safer X-ray contrast agents.[1–5] Most of them have focused on the modification of iodine-containing contrast molecules: encapsulation in[1–4] or linkage to[5] biocompatible organic molecules/polymers. A recent report by Hainfeld et al., however, demonstrated a possibility of Au NPs for an X-ray contrast agent.[6] They obtained the contrast images of the blood vessels and some organs of mice, by utilizing concentrated colloids of 1.9 nm diameter Au NPs as an X-ray contrast agent.

The nontoxic nature of bulk Au and relatively large (e.g., a few nm or bigger in diameter) Au NPs has been well documented,[7,8] but investigations on the toxicity of small Au NPs have been scarce. Recently, Schmit et al. reported the toxicity of very small Au NPs.[9,10] The authors observed strong cytotoxicity from 1.4 nm Au NPs, of which size is in a range for deteriorative interaction with

*Authors to whom correspondence should be addressed.

1533-4880/2007/7/7/26/8/$08 doi:10.1166/jnn.2007.601

the major grooves of deoxyribonucleic acids (DNAs). Thus, for medical applications, it is highly desirable to use the Au NPs larger than DNA grooves (typically less than 2 nm). In addition to the cytotoxicity problem, the Au NPs commensurate with or smaller may cause poor X-ray contrast because of their short vascular circulation time. However, very large Au NPs are also undesirable for medical applications because of the colloidal stability of the NPs decreasing with size and the difficulty in preparing homogeneous large (e.g., 40 nm or bigger in diameter) Au NPs.[11] Taking these into account, relatively large (here, between 10 and 40 nm in diameter) Au NPs seem to be suitable for an X-ray contrast agent application.

Like many medical applications of other colloidal NPs, the application of colloidal Au NPs for an X-ray contrast agent requires them being in a highly concentrated state to ensure high X-ray contrast. However, it is not a trifle to prepare stable and concentrated colloids of relatively large Au NPs, without proper surface modifications, because of their strong tendency to coagulate in concentrated state. One of the most useful and bio-friendly surface modifications is to encapsulate each Au NP in a silica shell because silica is biocompatible, feasible for further surface modifications,[8, 12–14] and has strong negative charge in biological environment.[15] The strong negative charge on the silica surfaces, contributing to electrostatic repulsion among the NPs, may enable to prepare highly stable and concentrated colloids of relatively large Au NPs.

There has been sparse documentation[16] on the concentrated colloids of silica-encapsulated Au ($Au@SiO_2$) NPs, even though plenty of documents[12, 17–22] have been available on the morphology and optical property of the NPs and their assemblies prepared from relatively low precursor concentration without enrichment. Unfortunately, no documentation is available on the colloidal stability and cytotoxicity of $Au@SiO_2$ NPs in biological environment, which are essential factors for medical applications. Here, as an effort to develop a new class of an effective and safe X-ray contrast agent, we report the colloidal stability in biological environment, *in vitro* cytotoxicity, and X-ray absorption of the concentrated colloidal $Au@SiO_2$ NPs (Au core diameter = ca. 15 nm, silica shell thickness = ca. 4 nm), along with their morphology and optical property.

2. EXPERIMENTAL DETAILS

2.1. Materials

Hydrogen tetrachloroaurate(III) tetrahydrate ($HAuCl_4 \cdot 4H_2O$), trisodium citrate dehydrate (Na_3-Cit), formaldehyde, 0.1 M phosphate buffered saline (PBS) solution were purchased from Wako Pure Chemicals. 3-Aminopropyl trimethoxysilane (APS) was supplied by Alfa-Aesar. Sodium silicate solution (ca. 27% SiO_2), DOWEX® 50WX4-400 ion-exchange resin, alpha-Minimum Essential Medium (MEM), and fetal bovine serum (FBS) were acquired from Sigma-Aldrich. Trypan blue and alamarBlue™ were provided by Gibco and Biosource, respectively. All chemicals were used as received. Milli-Q water (>18.2 MΩ cm) was used to prepare all aqueous solutions.

2.2. Preparation

The colloids of citrate-stabilized Au NPs were prepared according to the previously reported procedure.[11, 16] Briefly, 15 ml of mildly heated 1% Na_3-Cit solution was added to 282 ml of boiling 0.532 mM $HAuCl_4 \cdot 4H_2O$ solution under stirring; the final concentrations of Au^{3+} and $citrate^-$ were 0.5 and 0.17 mM, respectively. Silica shells were formed by adding 0.75 ml of 1 mM APS solution and 12 ml of 0.54 wt% sodium silicate solution (pH = 10.5–11, adjusted by using DOWEX® 50WX4-400 ion-exchange resin) to 300 ml of the colloids of citrate-stabilized Au NPs, followed by standing the mixtures (pH ≅ 8.5) for three days.[14, 16, 17, 21] The resulting colloids of $Au@SiO_2$ NPs were cleaned by a series of washing cycles: centrifugation (25,000 × g, 15 minutes), supernatant removal, and redispersion in water. Concentrated colloids were prepared by repeating the washing cycle, while gradually decreasing the amount of water for redispersion in each cycle (hereafter, referred as a 'mild enrichment'). A typical mild enrichment consisted of 4 washing cycles. Assuming that all Au^{3+} ions were used for producing Au NPs, the concentration of metallic Au in the concentrated colloids was 100 mM, 200 times higher than that in the colloids before the enrichment. Twice repetition of the mild enrichment was also performed to investigate its influence on the morphology and optical properties of the NPs. In this case, the final concentration of metallic Au in the resulting colloidal solution was also adjusted to 100 mM. For convenience, the metallic Au concentration was used for representing the concentration of Au or $Au@SiO_2$ NPs in colloids.

2.3. Instrument and Characterization

For characterizing the morphology of the NPs, the transmission electron microscopy (TEM) was performed with a JEOL JEM-2000 microscope operating at 200 KeV. The optical property of the colloidal NPs was characterized from their visible absorption spectra obtained with a Hitach U-2000 spectrophotometer. All optical spectra were obtained after adjusting metallic Au concentration to 0.5 mM. A Rigaku Rotaflex X-ray spectrometer was used for measuring X-ray transmittances of samples.

The stability of the concentrated colloidal NPs in biological environment was characterized based on the changes in their morphology and optical property upon transferring to 0.1 M PBS solution. The volume ratio of the colloid to the PBS solution was set to 0.5.

The viability and proliferation of rat fibroblast MC3T3-E1 cells, assessed by using a almarBlue™ assay, were used for evaluating the cytotoxicity of the NPs. For cell viability tests, the rat fibroblasts were incubated at 37° in 24-well plates using alpha-MEM containing 10% FBS (10^4 cells per well) and then various amount of the NPs (0.01–100 ppm) in water were added to each well. After further incubation at 37° for 24 hours, the viability of the rat fibroblasts was estimated based on the calorimetric detection of almarBlue™ reduction caused by live cells. For cell proliferation assays, both the rat fibroblasts and the NPs in water were seeded onto 24-well plates using alpha-MEM containing 10% FBS (10^4 cells per well) and then co-incubated for 24 hours. After cell fixing with formaldehyde and staining with trypan blue, stained cells (live cells) were counted under an optical microscope. In both the tests, the control sample was rat fibroblast MC3T3-E1 cells.

3. RESULTS AND DISCUSSION

3.1. Morphology

The citrate-induced reduction of Au^{3+} produced monodisperse spherical Au NPs with ca. 15 nm in diameter (Fig. 1(a)). The Au@SiO_2 NPs, prepared through silica coating in the basic silicate solution, are well separated each other without forming agglomerates, as shown in Figure 1(b). They have relatively homogeneous spherical silica shells of which thickness is ca. 4 nm.

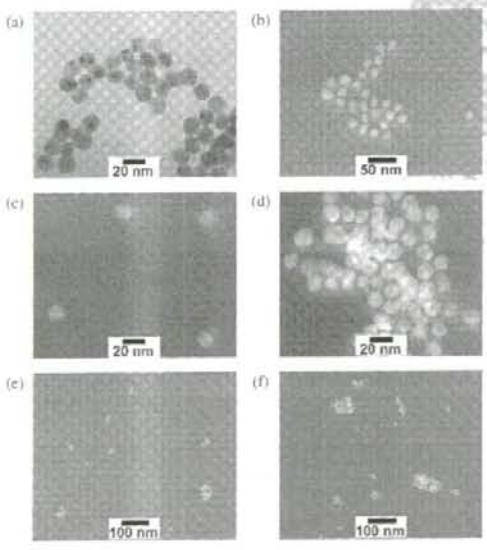

Fig. 1. TEM images of Au and Au@SiO_2 nanoparticles: (a) citrate-capped Au, (b) as-prepared Au@SiO_2 in water, (c) Au@SiO_2 in water after mild enrichment, (d) Au@SiO_2 after twice repetition of mild enrichment, (e) Au@SiO_2 in 0.1 M PBS solution after mild enrichment, and (f) Au@SiO_2 in 0.1 M PBS solution after twice repetition of mild enrichment. The concentrations of the NPs before and after the enrichments were equivalent to 0.5 and 100 mM metallic Au, respectively.

The concentrated colloidal Au@SiO_2 NPs, prepared through the mild enrichment, are well separated each other without forming agglomerates, even though some silica shells have minor shell damage such as detachment of some silica (Fig. 1(c)). The stability of these concentrated colloidal Au@SiO_2 NPs with minor shell damage (MSD) can be attributed to their high surface charge. In the experimental conditions of near neutral pH, the silica surfaces have high negative charge owing to the low isoelectric point of silica.[15] This enhances electrostatic repulsion among the NPs enough to stabilize them in the concentrated state.

The repetition of the mild enrichment exerted detrimental effect on the morphology of the Au@SiO_2 NPs. As shown in Figure 1(d), twice repetition of the enrichment resulted in profound shell damage (PSD): the silica shells seem to be inhomogeneous and little compact, compared with those obtained through the typical mild enrichment process. In part, they are loosely distributed among the Au NPs. Most of the NPs with PSD are poorly separated each other. In many cases, each NP is closely contacting with its immediate neighbor NPs through very thin silica barrier. Some NPs partially expose their Au cores or have big cores compose of two or more Au NPs. The formation of the big cores is related with the coagulation of the NPs with no or little silica. They have surface charge insufficient to prevent them from coagulation, because their surface charge diminishes with decreasing silica surface area.

3.2. Optical Property

As shown in Figures 2(a) and (b), the formation of 4 nm-thick silica shells caused a shift of Au surface plasmon resonance (SPR) peak from 519 to 523 nm. This red-shift by 4 nm is due to an increase in the local refractive index of the surrounding medium[17, 22] and is well in accordance with previous reports.[16, 17]

The optical property of the Au@SiO_2 NPs was strongly dependent on their morphology. As shown in Figure 2(c), the NPs with MSD show a SPR peak of which shape, intensity, and position are very similar to those of the NPs before the enrichment (Fig. 2(b)). The SPR peak of the NPs with PSD in Figure 2(d), however, is somewhat broad, weak, and red-shifted by 3 nm, compared with that of the NPs with MSD. These slight changes in optical property can be attributed to the close contact of the NPs and the existence of the NPs with bigger Au core.

3.3. Colloidal Stability in Biological Environment

In biological environment, the concentrated colloidal Au@SiO_2 NPs formed agglomerates of which size was strongly dependent on their initial morphology in water.

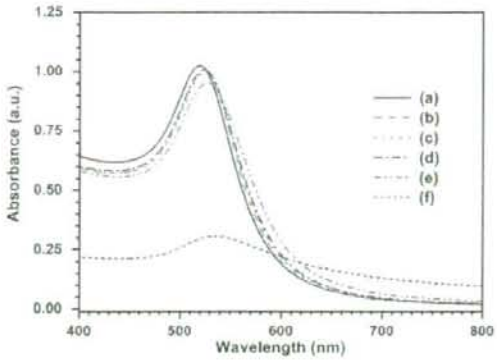

Fig. 2. Visible absorption spectra of Au and $Au@SiO_2$ nanoparticles: (a) citrate-capped Au, (b) as-prepared $Au@SiO_2$ in water, (c) $Au@SiO_2$ in water after mild enrichment, (d) $Au@SiO_2$ after twice repetition of mild enrichment, (e) $Au@SiO_2$ in 0.1 M PBS solution after mild enrichment, and (f) $Au@SiO_2$ in 0.1 M PBS solution after twice repetition of mild enrichment.

As shown in Figure 1(e), the morphology of the NPs with MSD in the PBS solution is very similar to that of the corresponding NPs in water, except for some agglomerates composed of relatively small number of the NPs. The formation of slightly more and bigger agglomerates of the NPs in the PBS solution is related with the flocculation caused by an increase in the ionic strength of the solution. Due to its high ion concentration, the PBS solution has stronger ionic strength than water. As the ionic strength of a solution increases, charge (opposite in sign) density around NPs increases. Because both ionic strength and charge density are inversely proportional to the square of the Debye shielding length, which is a measure of the strength of electrostatic potential damping from its pure value, electrostatic repulsion among the NPs is reduced and hence the NPs are destabilized with increasing ion concentration. Unlike those with MSD, the concentrated colloidal $Au@SiO_2$ NPs with PSD were unstable in the PBS solution: an immediate formation of precipitates was observed upon transferring to the solution. As shown in Figure 1(f), the TEM images of the NPs with PSD in the PBS solution show big agglomerates, along with some single NPs and small agglomerates composed of a few NPs with little or no silica shell. The big agglomerates consist of a few tens of the NPs, in which a couple of bigger Au NP cores are included. As discussed earlier, the formation of the big agglomerates of the NPs with PSD is related with the ionic strength of the PBS solution.

The optical property of the $Au@SiO_2$ NPs in PBS solution was also strongly influenced by their initial morphology: the NPs with MSD showed little change, whereas those with PSD experienced drastic change. The visible absorption spectrum of the NPs with MSD in the PBS solution (Fig. 2(e)) is very similar to that of the corresponding NPs in water (Fig. 2(c)): there is little difference in the shape, intensity, and position of the Au SPR peak. However, as shown in Figure 2(f), the NPs with PSD in the PBS solution shows a broad and weak Au SPR peak with very large background, compared with those in water (Fig. 2(d)). And their SPR peak is located at 534 nm, which is 7 nm longer than that in water. These optical observations imply the existence of various sizes of bigger NPs in the PBS solution and are well coincided with the previously described microscopic observations.

3.4. Cytotoxity

For medical applications, the $Au@SiO_2$ NPs should be biocompatible. Their biocompatibility was evaluated based on the viability and proliferation of rat fibroblast MC3T3-E1 cells. In general, 50% cell viability (or proliferation) is considered as a border of live or dead cells: materials giving 50% or higher cell viability (or proliferation) are biocompatible, while those with lower than 50% values are not. Figure 3 shows the viability and proliferation of the rat fibroblast cells after 24 hours incubation. In all the NP concentrations tested here, the rat fibroblast cells show more than 50% viability and proliferation. Even at a very high NP concentration of 100 ppm, the cell viability and proliferation are more than 70 and 60%, respectively. These confirm the biocompatibility of the $Au@SiO_2$ NPs. Especially the NPs show excellent biocompatibility at the concentration of 1 ppm or lower, as can be inferred from near 100% cell viability and proliferation.

3.5. X-ray Absorption

For achieving high X-ray contrast, contrast agents should show much stronger X-ray absorption (so, much lower X-ray transmittance) than human body, because X-ray contrasting ability relies on the differences in their X-ray

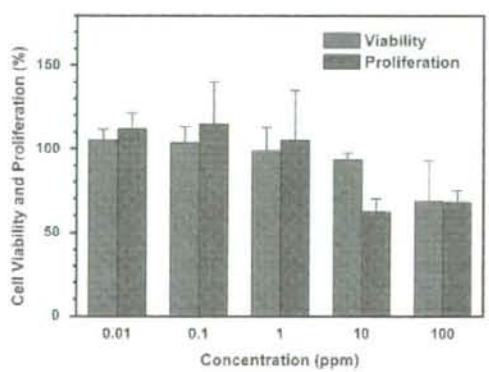

Fig. 3. Viability and proliferation of rat fibroblast MC3T3-E1 cells at various concentrations of $Au@SiO_2$ nanoparticles.

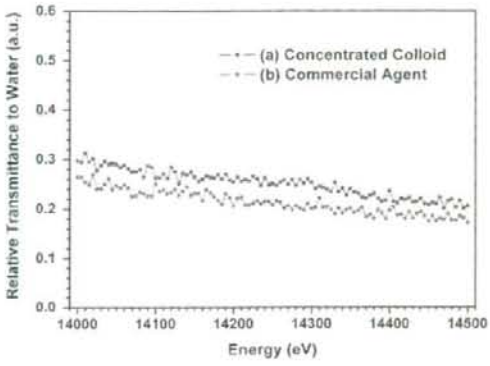

Fig. 4. Relative X-ray transmittances of (a) the concentrated colloid of $Au@SiO_2$ nanoparticles ([Au] = 100 mM) and (b) a commercial X-ray contrast agent (Iopamiron® 300). Relative transmittance = transmittance of sample/transmittance of water.

absorption. Therefore, the relative X-ray transmittance of a sample to water (a major constituent of human body) is a very important factor for evaluating its contrast ability. In general, materials with lower relative X-ray transmittance give better X-ray contrast.

Figure 4 shows the relative X-ray transmittances of the 100 mM colloidal $Au@SiO_2$ NPs and a commercial X-ray contrast agent (Iopamiron® 300). Average relative transmittance of the colloidal NPs is close to that of the commercial contrast agent. At Au L_I edge, the colloidal NPs shows the relative transmittance of ca. 0.237, which is very close to the calculated value of 0.231 based on X-ray mass attenuation coefficient of Au. Their slight discrepancy may be mainly due to the loss of the NPs during enrichments. Considering very low relative X-ray transmittance, comparable to that of a commercial contrast agent, the concentrated colloidal $Au@SiO_2$ NPs may be suitable for an X-ray contrast agent application.

4. SUMMARY AND CONCLUSIONS

As an effort to develop a new class of an effective and nontoxic X-ray contrast agent, highly concentrated colloidal $Au@SiO_2$ NPs were prepared and their colloidal stability in biological environment, *in vitro* cytotoxicity, and X-ray absorption were investigated. Each NP consists of ca. 15 nm diameter Au core and ca. 4 nm thick silica shell. The concentration of the concentrated colloidal NPs was equivalent to 100 mM metallic Au.

Highly stable and concentrated colloidal $Au@SiO_2$ NPs with MSD were prepared through the mild enrichment. The colloidal NPs with MSD were morphologically stable in concentrated state: they were well-separated each other, without forming agglomerates. The optical property of the concentrated colloidal NPs with MSD was very similar to that of the colloidal NPs before the enrichment: there was little change in the shape, intensity, and position of Au SPR peaks before and after the enrichment.

The concentrated colloidal $Au@SiO_2$ NPs with PSD were prepared through the repetition of the mild enrichment. The concentrated colloidal NPs with PSD showed the morphology somewhat different from that of the concentrated colloidal NPs with MSD: they were poorly separated each other and had very close contact with neighbor NPs. Due to their morphology, the NPs with PSD showed a Au SPR peak which is slightly broad, weak, and redshifted as compared with that of the NPs with MSD.

In biological environment, the stability of the concentrated colloidal $Au@SiO_2$ NPs was strongly dependent on their previous morphology in water. The concentrated colloidal NPs with MSD were stable in PBS solution, even though some small agglomerates were formed. However, the concentrated colloidal NPs with PSD were unstable in PBS solution: they formed big agglomerates, resulting in precipitation. These morphological differences affected their optical property. The colloidal NPs with MSD in PBS solution showed the Au SPR peak similar to that of the NPs in water, whereas those with PSD showed a very broad and red-shifted peak in PBS solution, as compared with those in water.

The $Au@SiO_2$ NPs are biocompatible. Both cell viability and proliferation assessments revealed no apparent cytotoxicity of the NPs even at the highest NP concentration tested here (100 ppm). Especially, at 1 ppm or lower, the NPs have an excellent biocompatibility: they showed near 100% cell viability and proliferation.

The concentrated colloidal $Au@SiO_2$ NPs showed strong X-ray absorption. Their relative transmittance to water, being inversely proportional to their X-ray contrast ability, is very low and close to that of a commercial contrast agent.

Taking into account their high colloidal stability in biological environment, excellent biocompatibility, and relative X-ray transmittance comparable to a commercial agent, the concentrated colloids of the $Au@SiO_2$ NPs, with relatively large Au core and little (or no) silica shell damage, are excellent materials for X-ray contrast agents.

Acknowledgments: This work was partially supported by Grant-in-Aid from the Ministry of Education, Science, Sports, and Culture, Japan. Authors wish to thank Prof. M. Konno of Tohoku University for his generosity in using the centrifuge.

References and Notes

1. U. P. Schmiedl, W. Krause, J. Leike, and A. Sachse, *Acad. Radiol.* 6, 164 (**1999**).
2. V. P. Torchilin, *Adv. Drug Deliv. Rev.* 54, 235 (**2002**).
3. D. R. Vera and R. F. Mattrey, *Acad. Radiol.* 9, 784 (**2002**).
4. C.-Y. Kao, E. A. Hoffman, K. G. Beck, R. V. Bellamkonda, and A. V. Annapragada, *Acad. Radiol.* 10, 475 (**2003**).
5. V. P. Torchilin, M. D. Frank-Kamenetsky, and G. L. Wolf, *Acad. Radiol.* 6, 61 (**1999**).

6. J. F. Hainfeld, D. N. Slatkin, T. M. Focella, and H. M. Smilowitz, *Br. J. Radiol.* 79, 248 (**2006**).
7. E. E. Connor, J. Mwamuka, A. Gole, C. J. Murphy, and M. D. Wyatt, *Small* 1, 325 (**2005**).
8. Z. P. Xu, Q. H. Zeng, G. Q. Lu, and A. B. Yu, *Chem. Eng. Sci.* 61, 1027 (**2006**).
9. Y. Liu, W. Meyer-Zaika, S. Franzka, G. Schmid, M. Tsili, and H. Kuhn, *Angew. Chem., Int. Ed.* 42, 2853 (**2003**).
10. M. Tsoli, H. Kuhn, W. Brandau, H. Esche, and G. Schmid, *Small* 1, 841 (**2005**).
11. G. Frens, *Nat. Phys. Sci.* 241, 20 (**1973**).
12. E. Mine, A. Yamada, Y. Kobayashi, M. Konno, and L. M. Liz-Marzán, *J. Colloid Interf. Sci.* 264, 385 (**2003**).
13. T. Schiestel, H. Brunner, and G. E. M. Tovar, *J. Nanosci. Nanotechnol.* 4, 504 (**2004**).
14. B. Rodríguez-González, A. Sánchez-Iglesias, M. Giersig, and L. M. Liz-Marzán, *Faraday Discuss.* 125, 133 (**2004**).
15. X. Cui, W.-C. Zin, W.-J. Cho, and C.-S. Ha, *Mater. Lett.* 59, 2257 (**2005**).
16. Y.-S. Park, L. M. Liz-Marzán, A. Kasuya, Y. Kobayashi, D. Nagao, M. Konno, S. Mamykin, A. Dmytruk, M. Takeda, and N. Ohuchi, *J. Nanosci. Nanotechnol.* 6, 3503 (**2006**).
17. L. M. Liz-Marzán, M. Giersig, and P. Mulvaney, *Langmuir* 12, 4329 (**1996**).
18. F. Caruso, M. Spasova, V. Salgueiriño-Maceria, and L. M. Liz-Marzán, *Adv. Mater.* 13, 1090 (**2001**).
19. F. García-Santamaría, V. Salgueiriño-Maceria, C. López, and L. M. Liz-Marzán, *Langmuir* 18, 4519 (**2002**).
20. Y. Yang, M. Hori, T. Hayakawa, and M. Nogami, *Surf. Sci.* 579, 215 (**2005**).
21. I. Tunc, S. Suzer, M. A. Correa-Duarte, and L. M. Liz-Marzán, *J. Phys. Chem. B* 109, 7597 (**2005**).
22. S. Liu and M. Han, *Adv. Funct. Mater.* 15, 961 (**2005**).

Received: 25 October 2006. Revised/Accepted: 22 November 2006.

Journal of
Nanoscience and Nanotechnology
Vol. 7, 3788–3791, 2007

Silicon Subiodide Clusters

Andriy Dmytruk[1,*], Yeon-Su Park[1], Atsuo Kasuya[1], Hideki Kikuchi[2], Masae Takahashi[2], Yoshiyuki Kawazoe[2], and Akira Watanabe[3]

[1] Center for Interdisciplinary Research, Tohoku University, Sendai, 980-8578, Japan
[2] Institute for Materials Research, Tohoku University, Sendai, 980-8577, Japan
[3] Institute of Multidisciplinary Research for Advanced Materials, Tohoku University, Sendai, 980-8577, Japan

Silicon subiodide clusters (Si_nI_m, $n = 1$–20) produced by laser ablation of bulk powder silicone tetraiodide have been investigated by time-of-flight mass spectroscopy and *ab initio* calculations. Both experimental results and theoretical calculations revealed a tendency to form different structures of the clusters depending on n: chain, ring, and cage structures for $n \leq 6$, $6 < n < 16$, and $n \geq 16$, respectively. The results show that iodine, similar to hydrogen, can be used for stable silicon cluster termination.

Keywords: Silicon, Iodide, Cluster.

1. INTRODUCTION

Small silicon clusters are the subject of research for many years because their electronic and optical properties are different from the bulk and important for semiconductor industries. Hydrogen terminated clusters have been studied extensively,[1,2] due to their conceptually simple structure. Iodine is another candidate for cluster termination. Since the bond energy of Si–I is low and close to that of Si–Si, as compared with Si–H,[2,3] iodine termination should affect less on the Si–Si bonds than hydrogen, allowing to study small silicon systems with less influence. No investigation on iodine-terminated silicon clusters has been reported hitherto.

Here, we present time-of-flight mass spectroscopic studies on silicon subiodide clusters produced by laser ablation and results of *ab initio* calculation on their structures.

2. EXPERIMENT AND CALCULATION

Silicon subiodide clusters were formed by the laser ablation of bulk powder SiI_4 in the Bruker Reflex III-T time-of-flight (TOF) mass spectrometer. The powder was produced by pounding SiI_4 crystals (Sigma-Aldrich) with a pestle in an agate mortar. The powder was mixed with small amount of solvent (hexane or acetonitrile, Aldrich). About 1 μl of the resulting suspension was dropped on a stainless steel target and then dried for the TOF measurements. All the above preparations were done in a glove box under nitrogen atmosphere to prevent SiI_4 from oxidation. The target was inserted in the mass spectrometer within a few seconds to minimize exposure of the sample in air. The chamber (flight tube) of the mass spectrometer was evacuated to about $5 \cdot 10^{-8}$ mbar. The spectrometer was equipped with a nitrogen laser which produced 4 ns pulses of 337.1 nm wavelength light with 300 μJ energy at 1–3 Hz repetition rate. Laser beam was passed though the controlled attenuator (typically 70–85% attenuation level was used) and focused into about 20 μm spot on the target. Produced ions were accelerated by 19 kV potential, separated in the flight tube, and detected by a microchannel plate detector. Positive or negative cluster ions were measured depending on the polarity of the accelerating potential. Typically the spectrum was recorded by accumulating the signal of about 500 laser shots.

Density functional theory (DFT) calculations were performed using Gaussian03 software package.[4] Geometries were fully optimized at the B3LYP/LANL2DZ level. Stationary points were confirmed to be a minimum by harmonic vibrational frequency analysis at each level.

3. RESULTS AND DISCUSSION

3.1. TOF Mass Spectrum Analysis

Figure 1 shows a TOF mass spectrum of positively charged $Si_nI_m^+$ clusters (laser attenuation level = 82%). The spectrum consists of a series of main peaks beginning with SiI_3^+ and equally separated by 281.9 Da, which corresponds to the mass of SiI_2 (281.8 amu). These main peaks, $Si_nI_{2n+1}^+$, are followed by weaker peaks separated by 27.99 Da, which corresponds to the mass of the main isotope of Si

*Author to whom correspondence should be addressed.

1533-4880/2007/7/3788/004 doi:10.1166/jnn.2007.020

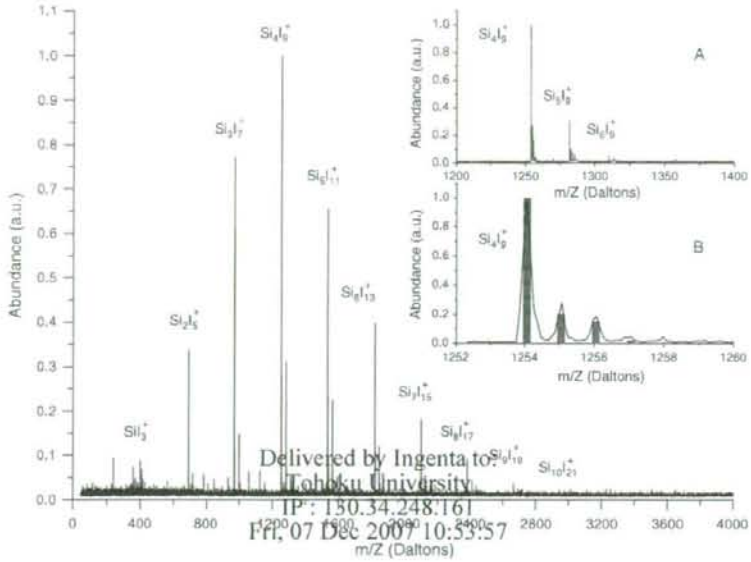

Fig. 1. Time-of-flight mass spectrum of positive ions produced by the laser ablation of SiI_4 bulk powder. Cluster assignments for main peaks in the series are shown. Inset A shows the spectral features near a main peak and their cluster assignment. Inset B shows isotopic distribution of $Si_4I_9^+$ cluster: Black line is the experimental spectrum, red bars show calculated isotopic distribution for the cluster.

(27.98 amu), as shown in the inset A in Figure 1. The structure of the peaks corresponds to the natural isotopic distribution of Si as indicated by red bars in the inset B in Figure 1. This proves the validity of the cluster assignments for the peaks on the mass spectrum. The mass spectrum of negatively charged $Si_nI_m^-$ clusters (not shown) is basically the same as that for positively-charged clusters, yet there are some differences: the most abundant positively charged cluster is $Si_4I_9^+$, while corresponding negatively charged one is $Si_2I_5^-$, with the series of peaks less extended to higher masses than the positive ions. This tendency is opposite to hydrogen terminated silicon clusters in silane plasma, where negatively charged clusters prevail at high masses,[2] probably due to the different polarity of preferential ionization. The similarity of mass spectra for positively and negatively charged ions is a good indication for the existence of the neutral clusters of the same structure.

Figure 2(a) shows a contour plot of all $Si_nI_m^+$ clusters assigned in Figure 1. Some rules for cluster stability are evident. Firstly, there is no cluster with $m > 2n+1$. Secondly, the most abundant clusters have $m = 2n+1$ (along the red line in Fig. 2). And thirdly, there are just few clusters with even values of m, while the most of the clusters have odd m values. These rules altogether lead us to the conclusion that the laser ablation of bulk powder SiI_4 produces mainly the chain structures ($Si_nI_{2n+1}^+$) in $n < 10$ region in which the clusters with $n = 4$ are the most abundant. They are similar to silicon hydride clusters, $Si_nH_{2n+1}^-$ with $n \leq 4$,[2] indicating that iodine termination has little influence on the silicon skeleton structure, similar to hydrogen termination.

Increasing the energy of laser pulses used for ablation of SiI_4 powder produces similar mass distribution with more Si rich clusters (i.e., with $m < 2n+1$) as shown in the contour plot obtained using laser attenuation level of 70% in Figure 2(b). Among them, those with $m < 2n-18$ (i.e., below the black line) can not be uniquely assigned, as masses of clusters Si_nI_m and $Si_{n+9}I_{m-2}$, for example, differ only by 2 amu. These two peaks are difficult to distinguish as they heavily overlap to each other by the natural isotope distribution, especially for large n.

For $n > 6$, $Si_nI_{2n+1}^+$ are found not the most abundant peaks. This can be seen by plotting the highest intensity peak for each n as displayed in Figure 3. This plot shows that $Si_nI_{4n/3+3}$ are most abundant for $6 < n < 16$, similar to $Si_nH_{4n/3}$ clusters for $n > 10$ in silane plasma.[2] At $n = 16$, the abrupt change of the most abundant ones occurs and more silicon rich structures begin to prevail. Such abrupt composition change was not observed for hydrogen terminated clusters (for $n < 40$) in silane plasma,[2] but was found at $n = 23$ for hydrogen terminated clusters produced by laser photolysis of disilane.[1] Unfortunately, it is difficult to explore the new tendency for $n > 16$ in detail as we reach the limit for unique cluster assignment. In all, the experimental results suggest the structural difference among the clusters depending on n: chains for $n \leq 6$, more compact forms for $n > 6$, and even more for $n \geq 16$.

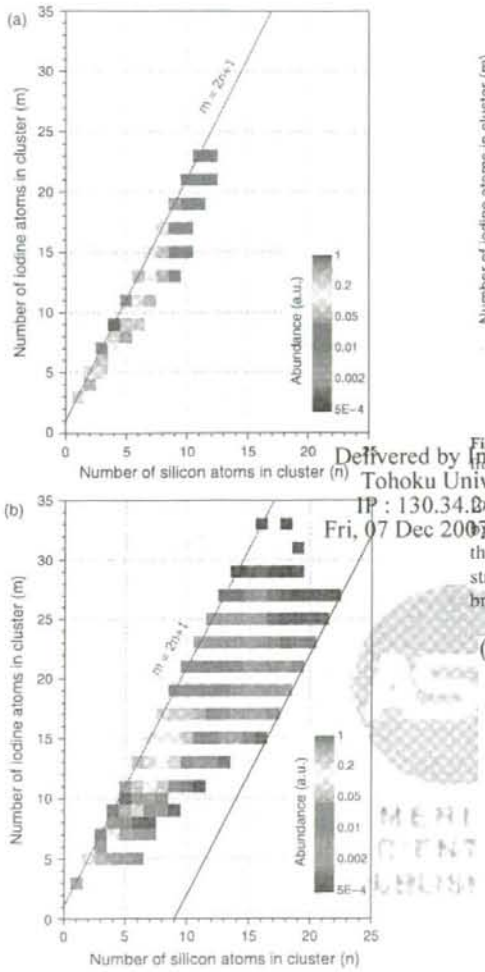

Fig. 2. Contour plots for the distribution of the silicon subiodide clusters produced at low (a) and high (b) laser energy.

3.2. Calculation Results

Mass spectroscopy cannot give information about cluster structures; it can only show the tendencies of cluster formation and their stability. To elucidate the cluster structures, we performed DFT calculations.

In $n \leq 6$ region, chain clusters $Si_nI_{2n+1}^+$ were observed in mass spectrum. For $n = 4$–6, several branched chain structures may be considered in addition to a straight chain structure. The number of branched structures sharply increases with n. We have compared the stability among the straight chains and all possible branched structures

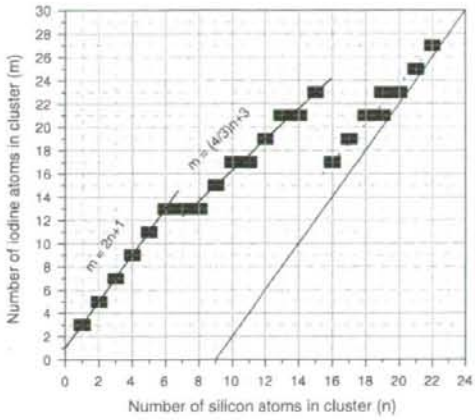

Fig. 3. Plots of the most abundant cluster at each n. Data were obtained from Figure 2(b).

from 3 to 14 and 5. The straight chains are more stable by 10853 kJ/mol ($n = 5$) than the branch chains at the B3LYP/LANL2DZ level. From $n = 3$, iodine-bridged structure appears. For example, silicons 2 and 4 are bridged by an iodine in the optimized chain structure of

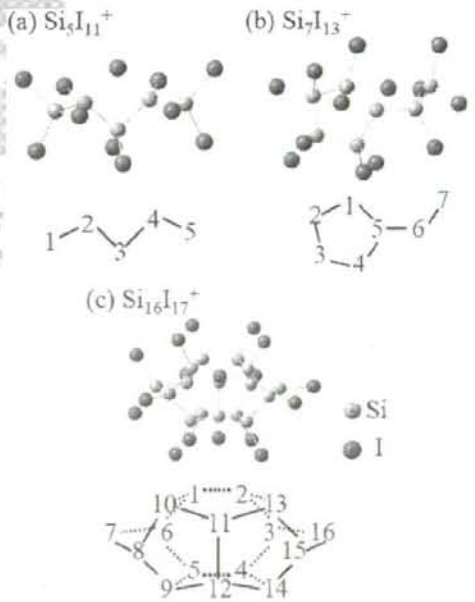

Fig. 4. Typical structures of chain (a), ring (b), and cage (c) clusters optimized at the B3LYP/LANL2DZ level. (a) R_{SiSi}(chain) = 2.39~2.40 Å, R_{SiSi}(bridge) = 2.42~2.43 Å. (b) R_{SiSi}(chain) = 2.41~2.42 Å, R_{SiSi}(ring) = 2.38~2.44 Å. (c) R_{SiSi}(5-membered ring) = 2.38~2.42 Å, R_{SiSi}(6-membered ring) = 2.39~2.40 Å, R_{SiSi}(edge) = 2.33~2.40 Å.